tured diamond emitter will most likely be used in the form of a thin coating, which can easily be applied to a large substrate by simple spray or printing techniques. The low threshold fields of 3 to 5 V/μm also imply that a gate voltage of 10 to 20 V, conveniently available from off-the-shelf complementary metal-oxide semiconductor drivers, will be adequate to control and address the display pixels.

Further, on the diamond cathode surface, a gate structure can be constructed by employing a simple "particle-mask" approach without using lithography. Such a robust, lithography-free (and therefore inexpensive) gate structure can have important technological impact. A layer of diamond particulates is first deposited on a substrate and activated by hydrogen plasma treatment (Fig. 4A). Fine and loose mask particles are then sprayed randomly over the cathode surface. A dielectric thin film is then deposited, followed by the deposition of the gate metal film. The mask particles shadow the areas directly underneath so that no dielectric or gate material is deposited on the cathode surface. The mask particles are then either brushed or blown away to reveal the gate apertures. As an example, we mixed fine aluminum particles with acetone and spray-coated them on a glass substrate. A layer of copper, about 1 μm thick, was then evaporated on the substrate. After gently brushing off the mask particles, apertures of about 2 to 4 μm in diameter are left in the copper film (Fig. 4B). The size, density, and distribution of the apertures can be controlled by selecting proper mask particles and processing schemes.

References and Notes

1. I. Brodie and C. A. Spindt, *Adv. Electron. Electron Phys.* **83**, 1 (1992).
2. F. J. Himpsel, J. A. Knapp, J. A. Van Vechten, D. E. Eastman, *Phys. Rev. B* **20**, 624 (1979).
3. J. Van der Weide and R. J. Nemanich, *Appl. Phys. Lett.* **62**, 1878 (1993).
4. C. Wang, A. Garcia, D. C. Ingram, M. Lake, M. E. Kordesch, *Electron. Lett.* **27**, 1459 (1991).
5. N. S. Xu, R. V. Latham, Y. Tzeng, *ibid.* **29**, 1596 (1993).
6. G. A. J. Amaratunga and S. R. P. Silva, *Appl. Phys. Lett.* **68**, 2529 (1996).
7. W. Zhu, G. P. Kochanski, S. Jin, L. Seibles, *J. Appl. Phys.* **78**, 2707 (1995).
8. N. Kumar, H. K. Schmidt, C. Xie, *Solid State Technol.* **38**, 71 (1995).
9. K. Okano, S. Koizumi, S. R. P. Silva, G. A. J. Amaratunga, *Nature* **381**, 140 (1996).
10. M. W. Geis, J. C. Twichell, T. M. Lyszczarz, *J. Vac. Sci. Technol. B* **14**, 2060 (1996).
11. B. B. Pate *et al.*, *J. Vac. Sci. Technol.* **19**, 349 (1981).
12. S. Koizumi, M. Kamo, Y. Sato, H. Ozaki, T. Inuzuka, *Appl. Phys. Lett.*, **71**, 1065 (1997).
13. W. Zhu, G. P. Kochanski, S. Jin, L. Seibles, *J. Vac. Sci. Technol. B* **14**, 2011 (1996).
14. M. Yoshikawa *et al.*, *Appl. Phys. Lett.* **67**, 694 (1995).
15. The field emission measurement was carried out in a vacuum chamber with a 10^{-8} torr base pressure at room temperature. As described previously (*7*), a voltage up to 2 kV was applied to a spherical-tipped molybdenum anode probe (tip radius of curvature ≅ 0.5 mm) to collect electrons emitted from the cathode diamond surface. A precision stepper controller (3.3 μm step size) was used to control the movement of the anode toward the cathode, and the emission current-voltage (*I-V*) characteristics were measured as a function of the anode-cathode distance. The obtained *I-V* data were analyzed using the Fowler-Nordheim theory (*22*), taking into consideration the variation of electrical field across the cathode surface and assuming a broad distribution in emission properties among the emitting tips (*13*). Capacitance was measured as the anode position changed to better determine the anode-cathode distance. A sphere-to-plane model was used to fit the capacitance data and estimate the position where the anode touched the cathode surface (*13*). The capacitance measurements also allowed problems—such as arcing, missteps of the probe, moving dust particles, or loose samples—to be detected, because they introduce discontinuities in an otherwise smooth capacitance-distance curve. The standard deviation of the capacitance about the fit corresponds to a 3 μm uncertainty out of a 100-μm spacing.
16. A sphere-on-cone model was adopted to derive the electrical field above the cathode surface (*23*), and a Fowler-Nordheim equation was then fit to the *I-V* data. The fitted parameters were used to interpolate or extrapolate the *I-V* characteristics of the emitters to a standard display pixel area (100 μm by 100 μm). The field required to produce an emission current density of 10 mA/cm^2 (that is, 1 μA over the pixel area, as is typically required for display applications) was then calculated and used as a figure of merit to compare various emitter samples. Note that we do not directly calculate the local fields on the tips of the emitters; instead, all of the field values are for the macroscopic electric field well above the cathode surface where the field is uniform and independent of the surface roughness. This macroscopic field is actually the relevant parameter for device applications. Using this field also allows us to avoid making strong assumptions about the emission physics, because the electronic properties of the emitters cannot be easily separated from the geometric field enhancement factors.
17. N. S. Xu, Y. Tzeng, R. V. Latham, *J. Phys. D* **26**, 1776 (1993).
18. J. D. Shovlin and M. E. Kordesch, *Appl. Phys. Lett.* **65**, 863 (1994).
19. M. W. Geis, J. C. Twichell, J. Macaulay, K. Okano, *ibid.* **67**, 1328 (1995).
20. A. A. Talin *et al.*, *ibid.* **69**, 3842 (1996).
21. D. Zhou *et al.*, *J. Appl. Phys.* **82**, 4546 (1997).
22. R. H. Fowler and L. W. Nordheim, *Proc. R. Soc. London Ser. A* **119**, 173 (1928).
23. J. He *et al.*, *Surf. Sci.* **246**, 348 (1991).
24. W. Zhu, G. P. Kochanski, S. Jin, unpublished data.

16 July 1998; accepted 16 October 1998

Coherent Optical Control of the Quantum State of a Single Quantum Dot

N. H. Bonadeo, J. Erland, D. Gammon, D. Park, D. S. Katzer, D. G. Steel*

Picosecond optical excitation was used to coherently control the excitation in a single quantum dot on a time scale that is short compared with the time scale for loss of quantum coherence. The excitonic wave function was manipulated by controlling the optical phase of the two-pulse sequence through timing and polarization. Wave function engineering techniques, developed in atomic and molecular systems, were used to monitor and control a nonstationary quantum mechanical state composed of a superposition of eigenstates. The results extend the concept of coherent control in semiconductors to the limit of a single quantum system in a zero-dimensional quantum dot.

Semiconductor quantum dots (QDs) are nanoscopic quantum structures (*1*) that allow electronic properties to be tailored through quantum confinement. Advances in optical spectroscopy techniques have revealed the distinctive features of these nanostructures, including atomic-like spectra with discrete and extraordinarily sharp spectral lines (*2–4*). However, the similarities between atoms and QDs suggest the possibility of even greater opportunities. More specifically, we can consider the possibility of using coherent optical interactions to coherently engineer the wave function. Such proposals have been envisioned for implementation of various schemes for quantum computation and coherent information processing and transfer in which it is important to address and coherently control individual quantum units (*5*). In addition, it might be possible to extend earlier demonstrations of coherent control of semiconductor heterostructures such as photocurrent (*6*) and terahertz radiation (*7*) to a single quantum dot.

Coherent control of quantum mechanical processes and wave function engineering in atomic and molecular systems have reached an advanced level of understanding including control of molecular chemical reactions (*8*), selective photodissociation of molecules (*9*),

N. H. Bonadeo, Harrison M. Randall Laboratory of Physics and Center for Ultrafast Optical Science, University of Michigan, Ann Arbor, MI, 48109, USA. J. Erland, Harrison M. Randall Laboratory of Physics, University of Michigan, Ann Arbor, MI, 48109, USA. D. Gammon, D. S. Katzer, D. Park, Naval Research Laboratory, Washington, DC 20375, USA. D. G. Steel, Harrison M. Randall Laboratory of Physics and Electrical Engineering and Computer Science Department, University of Michigan, Ann Arbor, MI, 48109, USA.

*To whom correspondence should be addressed.

generation of nonclassical motional states in ions (*10*), and localization of electronic wavepackets in atoms (*11*). More recent work has resulted in the full characterization of the amplitude and phase of an electronic wave function (*12*). These concepts have been extended to control the state of excitation in semiconductors including control of photocurrent direction (*6*) and charge oscillations leading to terahertz radiation (*7*) as indicated above, as well as electron-phonon scattering (*13*), cyclotron emission (*14*), and population and orientation of excitons (*15*). In contrast to the higher dimensional semiconductor systems, QDs offer the possibility of coherent manipulation of a single localized quantum system in a way similar to that achieved in atoms but with the technological advantages of a solid-state system. The well-defined localized states of this system make it possible to use the results of coherent control in semiconductors to enable wave function engineering of specific target states, a result of both fundamental and practical significance.

Here, we apply the methodology developed in atomic and molecular systems to extend the studies in higher dimensional semiconductor structures to the ultimate quantum limit of a single zero-dimensional QD. The results demonstrate coherent optical control of an exciton wave function and take the first step toward wave function engineering in these systems. In particular, we coherently control the state of excitation in a QD, measure the autocorrelation of the wave function using wave packet interferometry, and manipulate the relative phases of the eigenstates in a quantum superposition of states to generate a simple target wave function.

The QDs investigated in these experiments are naturally formed by width fluctuations in a 4-nm quantum well layer of GaAs sandwiched between 25-nm $Al_{0.3}Ga_{0.7}As$ barriers. Previous measurements show that the QDs are shaped as elliptical disks oriented along the [110] axes with a lateral size ~10 times larger than the 4-nm height (*16*). The lateral potential depth is ~8 meV. An exciton in an isolated QD is probed by exciting through a 500-nm-diameter aperture in a 100-nm-thick Al mask deposited directly on the sample surface. Photoluminescence (PL) and photoluminescence excitation (PLE) spectra of these structures exhibit extremely sharp resonances and atomic-like excitation spectra (*17*). Linear and coherent nonlinear spectroscopy performed in these single QDs (*3*, *18*) show that the linewidths are homogeneously broadened, with the linewidth primarily lifetime-limited. Polarization studies reveal that each resonance is composed of two optically accessible states orthogonally polarized (X' and Y', parallel to the [110] axes) where the degeneracy has been lifted by the QD elongation (*16*, *19*). As a consequence of a long spin-flip relaxation time observed in these dots, the PL emission remains highly polarized because the exciton relaxes to the ground state of the crystal through photon emission before undergoing a spin flip (*16*).

The PL and PLE spectra of the QD for these studies are shown in Fig. 1A (Y'-polarized, all data obtained at $T = 6$ K). We focus our transient studies on the strong absorption resonance (state $|E_1\rangle$). A detailed view of the fine structure of $|E_1\rangle$ showing the X' ($|E_{1X'}\rangle$)– and Y' ($|E_{1Y'}\rangle$)–polarized states is presented in Fig. 1B. A Lorentzian fit to the homogeneous linewidth gives $\hbar\gamma \sim 17$ μeV for both states (corresponding to a dephasing time, that is, time scale for loss of quantum coherence, of $T_2 = \gamma^{-1} \sim 39$ ps) and an energy splitting $E_{1X'} - E_{1Y'} = \hbar\delta \sim 60$ μeV. The $|E_0\rangle$ state (~2.6 meV below $|E_1\rangle$) is also a doublet, but is not spectrally resolved in these measurements.

Coherent optical control and wavepacket interferometry were achieved by using a sequence of two phase-locked laser pulses delayed in time (*20*–*23*). The laser is tuned to the $|E_1\rangle$ state and has a 5-ps pulsewidth. The laser bandwidth is broad compared with the $|E_1\rangle$ splitting but sufficiently narrow so as not to excite other states (Fig. 1A). The pulses create a population at state $|E_1\rangle$ which, on the basis of earlier studies (*3*, *24*), decays primarily by acoustic phonon emission to the state $|E_0\rangle$. Hence, the state of excitation of $|E_1\rangle$ can be monitored through the PL from the state $|E_0\rangle$ according to the energy level diagram shown in Fig. 1C.

Phase-locking of the relative phase and control of the delay of the laser pulses is accomplished by sending a laser pulse through a subwavelength-stable Michelson interferometer with a coarse (τ_c) and fine delay adjustment (τ_f) provided by a mechanical and piezoelectric translation stage, respectively (Fig. 2, top inset). The total delay is $\tau = \tau_c + \tau_f$. A quarter wave plate sets the relative polarization of the pulses, and a polarization rotator controls the relative polarization of the pulses with respect to the eigenaxes of the sample, X' and Y'. The polarization of the PL is analyzed either along the Y' axis or at 45°.

To understand the quantum mechanical basis for coherent optical control and wavepacket interferometry, we consider the interaction of two optical pulses with the QD at time $t = 0$ and $t = \tau$, respectively. In the low-excitation limit (only single-photon processes are considered), the total excited state wave function is a coherent superposition of the excited state wave function created by both pulses:

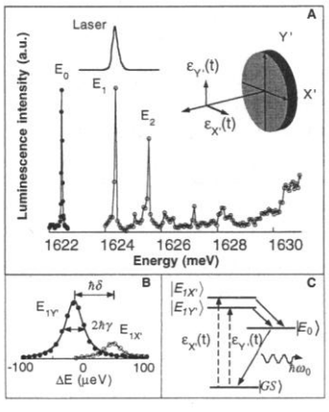

Fig. 1. (**A**) PL (●) and PLE (○) spectra of the $|E_0\rangle$ state obtained with Y'-polarized continuous-wavelength excitation showing various discrete states and a continuum. Also shown is the laser spectrum of the pulse used for the time domain experiments and a diagram of QD axes. (**B**) A detailed plot of the fine-structure PLE spectrum of state $|E_1\rangle$ showing the splitting of the X' ($|E_{1X'}\rangle$)– and Y' ($|E_{1Y'}\rangle$)–polarized states. The curves are a Lorentzian fit to the data. (**C**) An energy diagram of the optical transitions involved in this experiment. The dashed lines represent polarized optical excitation and the solid lines represent decay by phonon ($|E_1\rangle \rightarrow |E_0\rangle$) and photon (PL from $|E_0\rangle \rightarrow |GS\rangle$) emission.

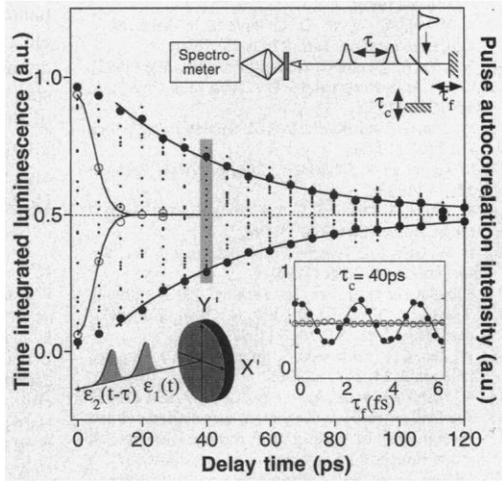

Fig. 2. The amplitude of the oscillation in PL as a function of delay (large filled circles) when both pulses are copolarized along the y' axis, thus exciting just the $|E_{1Y'}\rangle$ state. This measures the autocorrelation function of the excited state wave function. (**Lower right inset**) An expanded view around $\tau_c = 40$ ps (corresponding to the shadowed region) of the small filled circles showing the oscillation in PL as a function of τ_f. The large filled circles in the main figure are determined from a fit of the amplitude of the oscillation as a function of τ_f. The amplitude of the oscillation shows an exponential decay over long times. The autocorrelation function of the pulse is also plotted for reference (open circles). (**Top inset**) Schematic of the experimental setup. (**Lower left inset**) Field polarization of the optical pulses relative to the crystal axes.

$$|\Psi(t,\tau)\rangle = |\phi^{(1)}(t)\rangle + |\phi^{(2)}(t-\tau)\rangle \quad (1)$$

where $|\phi^{(i)}(t)\rangle$ is the excited state wave function generated by the pulse i. Equation 1 represents the sum of two quantum mechanical paths connecting the initial and final states. Quantum interference between these two paths is observed by measuring the excited state population generated by the pulse pair as a function of the time delay between pulses. The population is proportional to

$$\int_{-\infty}^{\infty} \langle\Psi(t,\tau)|\Psi(t,\tau)\rangle dt$$

$$= \int_{-\infty}^{\infty} \left[\langle\phi^{(1)}|\phi^{(1)}\rangle + \langle\phi^{(2)}|\phi^{(2)}\rangle + 2\Re e[\langle\phi^{(1)}(t)|\phi^{(2)}(t-\tau)\rangle]\right] dt \quad (2)$$

As we change the delay between the pulses, the first two terms in this expression remain unchanged whereas the last term oscillates as the interference between the two quantum mechanical paths goes from constructive to destructive. This process is analogous to Young's double-slit experiment where interference takes place because we are unable to distinguish between different photon paths that lead to the detector. In our experiment, the quantum interference can be controlled by changing the delay and, as we see below, the polarization between the pulses.

The last term in Eq. 2 is the cross-correlation function of the excited state wave function generated by the first and second pulses. A measurement of this function yields important information about the temporal evolution of the wave function and is the basis for wavepacket interferometry (*12*). A complete characterization (amplitude and phase) of the wave function generated by one pulse can be obtained if the wave function generated by the other pulse is known. In case both pulses are identical, Eq. 2 becomes the autocorrelation function of the excited state wave function and allows us to extract the decoherence time of the system as well as the dynamics of the wave function's temporal evolution. We present three experiments with increasing degrees of complexity in the final-state wave function.

In the simplest experiment, both pulses [$\varepsilon_1(t)$ and $\varepsilon_2(t)$] propagating in the z direction) are copolarized along the Y' axis (Fig. 2, lower left inset). The PL polarization is also analyzed along the Y' axis. The excited state wave function created by each pulse is $|\phi^{(1)}(t)\rangle = |\phi^{(2)}(t)\rangle = e^{-\omega_{1Y'}t}c_{1Y'}|E_{1Y'}\rangle$. Figure 2 shows the amplitude of the resulting oscillation in the PL (large filled circles), that is, the quantum interferogram (*20*), as a function of the time delay between pulses as well as the autocorrelation function of the laser pulse (open circles). An expanded view of the oscillation (small filled circles) at $\tau_c = 40$ ps is shown in the lower right inset. The oscillation as a function of τ corresponds to constructive and destructive interference between $|\phi^{(1)}(t)\rangle$ and $|\phi^{(2)}(t-\tau)\rangle$ of Eq. 2. The plot shows that even for pulse delays much longer than the pulse duration, a strong oscillation in the PL intensity persist. The absence of optical interference at those time delays allows us to conclude that the oscillation in the PL intensity is purely quantum mechanical in nature. These oscillations are analogous to the Ramsey interference fringes observed in atomic and molecular systems (*20*, *22*, *25*).

The reduction in the amplitude of the oscillation for increasing pulse delay observed in Fig. 2 is a consequence of the dephasing processes caused by interactions such as elastic and inelastic scattering that perturb the wave function of the system. A calculation with the density matrix equations, which includes dephasing processes that lead to loss of the optically induced quantum coherence, shows that the time-integrated PL intensity, as a function of the delay between pulses is $I(\tau) \propto (1/2)[1 + \cos(\omega_{1Y'}\tau)\exp(-\tau/T_2)]$ where T_2 is the dephasing rate. As seen in Fig. 2, the envelope of the data fits an exponential decay and leads to a direct measurement of T_2 giving ~40 ps, in excellent agreement with the value obtained from the PLE linewidth ($\gamma^{-1} = 39$ ps). Separate measurements show that the loss of coherence in this structure is likely due to acoustic phonon relaxation from $|E_1\rangle$ to $|E_0\rangle$ and radiative recombination rather than elastic scattering (*3*, *18*). Loss of coherence limits the ability to coherently manipulate the wave function for time scales $> T_2$.

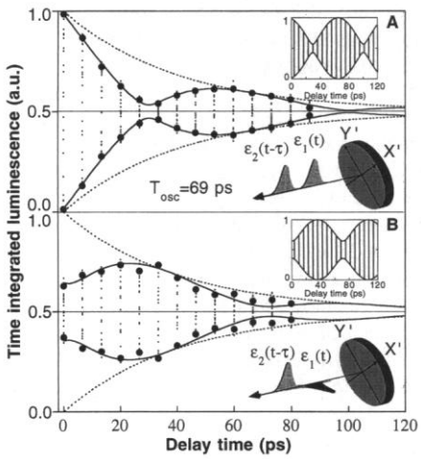

Fig. 3. (**A**) The excited state autocorrelation function of the excited state wave function, as in Fig. 2 but for both pulses copolarized and rotated to equally excite both the $|E_{1X'}\rangle$ and $|E_{1Y'}\rangle$ states. The temporal evolution shows oscillations as the wave function oscillates between the two orthogonal states. The long time scale oscillation period corresponds to the inverse of the difference frequency between the two optical transitions. (**B**) The cross-correlation function between two excited state wave functions generated by orthogonally polarized optical pulses. The relative phase of the two superposition of states produced by each pulse differs by π. The top inset in each figure shows the calculated oscillations in the absence of dephasing. Lower insets show the field polarization of the optical pulses relative to the crystal axes.

In the second experiment we rotate the polarization of the copolarized pulse sequence with respect to the sample's eigenaxes (Fig. 3A, lower inset), and generate a nonstationary (time-dependent) wave function composed of a superposition of states $|E_{1X'}\rangle$ and $|E_{1Y'}\rangle$. The polarization of the pulses is adjusted to compensate for the difference in the oscillator strength of the X' and Y' transition to equally excite both states. The PL is detected near 45° relative to the Y' axis to ensure that the emission is proportional to the total population and not just the population in one eigenstate. The wave function generated by each pulse is now $|\phi^{(1)}(t)\rangle = |\phi^{(2)}(t)\rangle = e^{-i\omega_{1X'}t}c_{1X'}|E_{1X'}\rangle + e^{-i\omega_{1Y'}t}c_{1Y'}|E_{1Y'}\rangle$ where the coefficients $c_{1X'}$ and $c_{1Y'}$ are similar in magnitude and are defined to be real. The dynamics of the nonstationary state of the excited state wave function are seen in the quantum interferogram as a slow oscillation superimposed on the rapid oscillation shown in the lower right inset of Fig. 2. More specifically, the autocorrelation function of the excited state wave function (Eq. 2), shows how it oscillates between two orthogonal states, $|E_{1X'}\rangle + |E_{1Y'}\rangle$ and $|E_{1X'}\rangle - |E_{1Y'}\rangle$ as the envelope function goes from a maximum to a minimum as a function of time. The slow oscillation period, $T_{osc} = 69$ ps, is in excellent agreement with the fine structure splitting $T_{osc} = 2\pi/\delta$ (Fig. 1B). As in Fig. 2, the exponential decay of the envelope is due to the loss of coherence.

In the third experiment we control the relative quantum phase of the superposition of states to demonstrate the feasibility of producing a general target wave function (in more complex experiments, more than two eigenstates and their relative phases would be involved in determining a target wave function). To accomplish this, we rotate the polarization of the second pulse by $\pi/2$ and generate a wave function where the relative quantum phase is shifted by π relative to that created by the first pulse. Following Eq. 1, the first pulse leads to $|\phi^{(1)}(t)\rangle = c_{1X'}^{(1)}e^{-i\omega_{1X'}t}|E_{1X'}\rangle + e^{-i\omega_{1Y'}t}c_{1Y'}^{(1)}|E_{1Y'}\rangle$ whereas the second pulse leads to $|\phi^{(2)}(t)\rangle = c_{1X'}^{(2)}e^{-i\omega_{1X'}t}|E_{1X'}\rangle + e^{-i\omega_{1Y'}t}c_{1Y'}^{(2)}|E_{1Y'}\rangle e^{i\pi}$. The quantum interferogram shown in Fig. 3B now reports on the cross-correlation function of the two wave functions as described by Eq. 2. The plot shows a minimum at $t = 0$ and a maximum at $t = T_{osc}/2$, opposite to that observed in the autocorrelation, as ex-

pected (that is, π out of phase). This difference becomes even more apparent when we compare the top insets in Fig. 3, A and B, which represent the calculated interferogram amplitudes in the absence of dephasing for the parameters obtained from fitting the data points (*26*).

The excited state coherence of the artificial "atom" studied here has a decoherence time of 40 ps, which is short compared with atomic coherence times, thus limiting the use of these particular QDs for quantum logic. However, very long electronic spin coherence in semiconductors has recently been measured (*27*). Furthermore, QD structures with stronger confinement are expected to have reduced coupling to phonons (*28*) and reduced spontaneous radiative emission (*29*), and may well have much longer intrinsic coherence times. In addition, doping of dots may result in isolated impurity states with long coherence times associated with more complex states of excitation such as demonstrated in atomic systems (*30*). Such progress should allow the use of more complicated sequences of control pulses during the coherence time, such as those necessary for performing quantum logic (*5*) or other coherently controlled processes.

The measurements show that we have successfully demonstrated coherent optical control of the quantum state of a single dot and thus have taken this technique to the ultimate quantum limit. We show that we can extend such an experiment to include more than one excited state and monitor the wave function as it oscillates between two orthogonal states by measuring the autocorrelation function. Finally, we show the feasibility of generating a target wave function by demonstrating control over the quantum mechanical phase of the superposition of states. This work establishes the basic tools for developing more sophisticated control and for creating a more complex wave function such as achieved in atomic systems.

Reference and Notes

1. A. P. Alivisatos, *Science* **271**, 933 (1996).
2. K. Brunner *et al.*, *Phys. Rev. Lett.* **73**, 1138 (1994); H. F. Hess *et al.*, *Science* **264**, 1740 (1994).
3. D. Gammon *et al.*, *Science* **273**, 87 (1996).
4. G. Schedelbeck, W. Wegscheider, M. Bichler, G. Abstreiter, *ibid.* **278**, 1792 (1997); S. A. Empedocles and M. G. Bawendi, *ibid.*, p. 2114; D. Gammon *et al.*, *ibid.* **277**, 85 (1997); J. Hasen *et al.*, *Nature* **390**, 54 (1997); E. Dekel *et al.*, *Phys. Rev. Lett.* **80**, 4991 (1998); L. Landin *et al.*, *Science* **280**, 262 (1998).
5. S. Lloyd, *Science* **261**, 1569 (1993); A. Barenco, D. Deutsch, A. Ekert, R. Jozsa, *Phys. Rev. Lett.* **74**, 4083 (1995); A. Ekert and R. Jozsa, *Rev. Mod. Phys.* **68**, 733 (1996).
6. A. Hache *et al.*, *Phys. Rev. Lett.* **78**, 306 (1997).
7. P. C. M. Planken *et al. Phys. Rev. B* **48**, 4903 (1993).
8. R. N. Zare, *Science* **279**, 1875 (1998); W. S. Warren, H. Rabitz, M. Dahleh, *ibid.* **259**, 1581 (1993).
9. F. Wang, C. Chen, D. S. Elliot, *Phys. Rev. Lett.* **77**, 2416 (1996).
10. D. M. Meekhof *et al.*, *ibid.* **76**, 1796 (1996).
11. J. A. Yeazell and C. R. Stroud Jr., *ibid.* **60**, 1494 (1988).
12. T. C. Weinacht, J. Ahn, P. H. Bucksbaum, *ibid.* **80**, 5508 (1998); *Nature*, in press.
13. M. U. Wehner, M. H. Ulm, D. S. Chemla, M. Wegener, *ibid.*, p. 1992.
14. P. G. Huggard *et al.*, *Appl. Phys. Lett.* **71**, 2647 (1997).
15. A. P. Heberle, J. J. Baumberg, K. Kohler, *Phys. Rev. Lett.* **75**, 2598 (1995); X. Marie *et al.*, *ibid.* **79**, 3222 (1997).
16. D. Gammon *et al.*, *ibid.* **76**, 3005 (1996).
17. D. Gammon, E. S. Snow, D. S. Katzer, *Appl. Phys. Lett.* **67**, 2391 (1995).
18. N. H. Bonadeo *et al.*, *Phys. Rev. Lett.* **81**, 2759 (1998).
19. S. V. Goupalov, E. L. Ivchenko, A. V. Kavokin, *J. Exp. Theor. Phys.* **86**, 388 (1998).
20. N. F. Scherer *et al.*, *J. Chem. Phys.* **95**, 1487 (1991).
21. H. Metiu and V. Engel, *J. Opt. Soc. Am. B* **7**, 1709 (1990); J. T. Fourkas *et al.*, **6**, 1905 (1989).
22. F. Spano, M. Haner, W. S. Warren, *Chem. Phys. Lett.* **135**, 97 (1987).
23. V. Blanchet, C. Nicole, M.-A. Bouchene, B. Girard, *Phys. Rev. Lett.* **78**, 2716 (1997).
24. U. Bockelmann, *Phys. Rev. B* **48**, 17637 (1993).
25. M. M. Salour and C. Cohen-Tannoudji, *Phys. Rev. Lett.* **38**, 757 (1977); L. D. Noordam, D. I. Duncan, T. F. Gallagher, *Phys. Rev. A* **45**, 4734 (1992).
26. Because the X'- and Y'-oscillator strengths are different, complete cancellation is not observed at the nodes.
27. J. M. Kikkawa, I. P. Smorchkova, N. Samarth, D. D. Awschalom, *Science* **277**, 1284 (1997); J. M. Kikkawa and D. D. Awschalom, *Phys. Rev. Lett.* **80**, 4313 (1998).
28. U. Bockelmann and G. Bastard, *Phys. Rev. B* **42**, 8947 (1990).
29. D. S. Citrin, *Phys. Rev. B* **47**, 3832 (1993).
30. T. Mossberg, A. Flusberg, R. Kachru, S. R. Hartman, *Phys. Rev. Lett.* **42**, 1665 (1979); B. Young, M. Kasevich, S. Chu, in *Atom Interferometry*, P. R. Berman, Ed. (Academic Press, New York, 1997).

31. We thank P. H. Bucksbaum and R. Merlin for stimulating discussions. Supported by U.S. Army Research Office, Air Force Office of Scientific Research, Office of Naval Research and NSF (Center for Ultrafast Optical Science). J.E. was supported by the Danish Research Council.

10 July 1998; accepted 16 September 1998

Photonic Band Gap Guidance in Optical Fibers

J. C. Knight, J. Broeng,* T. A. Birks, P. St. J. Russell

A fundamentally different type of optical waveguide structure is demonstrated, in which light is confined to the vicinity of a low-index region by a two-dimensional photonic band gap crystal. The waveguide consists of an extra air hole in an otherwise regular honeycomb pattern of holes running down the length of a fine silica glass fiber. Optical fibers based on this waveguide mechanism support guided modes with extraordinary properties.

Photonic band gap (PBG) structures offer the opportunity to design new optical properties into existing materials by wavelength-scale periodic microstructuring of the material morphology (*1*). In three-dimensionally periodic PBG materials, waves of certain frequencies cannot enter into or propagate through the material (*1*). In two-dimensionally periodic materials, there can be ranges of the propagation constant normal to the periodic plane (β) where propagation is forbidden (*2, 3*). One potential application of such materials is a type of optical waveguide where light is confined by surrounding it with a band gap material (*4*). Two-dimensionally periodic structures in the form of long, fine silica fibers that have a regular array of tiny air holes running down their length (*3, 5–8*) constitute artificial two-dimensional "crystals" with lattice constants on the order of micrometers. We previously demonstrated an optical fiber waveguide based on total internal reflection from this periodic material—a waveguiding mechanism very similar to that in conventional optical fibers (albeit with some remarkable features) (*5–8*). We now report the realization and demonstration of a far more radical optical fiber design, based on light confinement by the PBG effect.

Our fabrication process is related to that reported by Tonucci *et al.* (*9*) and involves stacking a few hundred solid silica rods and silica capillary tubes by hand in a hexagonal arrangement to form a fiber preform, which is then drawn down at a temperature of around 2000°C to a fiber with a diameter of about 40

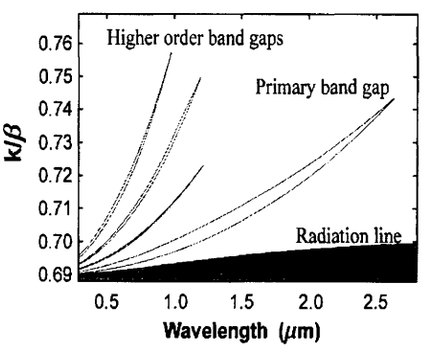

Fig. 1. Computed band gaps in the air-silica honeycomb lattice being discussed here. The parameters used in the computation were a nearest hole spacing of 1.9 μm and an air hole diameter of 0.55 μm.

Optoelectronics Group, Department of Physics, University of Bath, Claverton Down, Bath BA2 7AY, UK.

*Visiting from the Department of Electromagnetic Systems, Technical University of Denmark, 2800 Lyngby, Denmark.